Monthly Notices
of the
ROYAL ASTRONOMICAL SOCIETY

MNRAS **496,** 169–181 (2020)
Advance Access publication 2020 June 2

doi:10.1093/mnras/staa1499

Validating scattering-induced (sub)millimetre disc polarization through the spectral index, wavelength-dependent polarization pattern, and polarization spectrum: the case of HD 163296

Zhe-Yu Daniel Lin [1]★ Zhi-Yun Li,[1] Haifeng Yang [2] Leslie Looney,[3] Ian Stephens[4] and Charles L. H. Hull[5,6]†

[1]*Department of Astronomy, University of Virginia, 530 McCormick Rd., Charlottesville 22904, Virginia, USA*
[2]*Institute for Advanced Study, Tsinghua University, Beijing 100084, People's Republic of China*
[3]*Department of Astronomy, University of Illinois at Urbana-Champaign, Urbana IL 61801, USA*
[4]*Harvard-Smithsonian Center for Astrophysics, 60 Garden Street, Cambridge, MA 02138, USA*
[5]*National Astronomical Observatory of Japan, NAOJ Chile Observatory, Alonso de Córdova 3788, Vitacura, Santiago, Chile*
[6]*Joint ALMA Observatory, Alonso de Córdova 3107, Vitacura, Santiago, Chile*

Accepted 2020 May 27. Received 2020 May 17; in original form 2019 December 22

ABSTRACT

A number of young circumstellar discs show strikingly ordered (sub)millimetre polarization orientations along the minor axis, which is strong evidence for polarization due to scattering by ∼0.1 mm-sized grains. To test this mechanism further, we model the ALMA dust continuum and polarization data of HD 163296 using RADMC-3D. We find that scattering by grains with a maximum size of 90 μm simultaneously reproduces the polarization observed at Band 7 and the unusually low spectral index ($\alpha \sim 1.5$) between Bands 7 and 6 in the optically thick inner disc as a result of more efficient scattering at the shorter wavelength. The low spectral index of ∼2.5 inferred for the optically thin gaps is reproduced by the same grains, as a result of telescope beam averaging of the gaps (with an intrinsic $\alpha \sim 4$) and their adjacent optically thick rings (where $\alpha \lesssim 2$). The tension between the grain sizes inferred from polarization and spectral index disappears because the low α values do not require large mm-sized grains. In addition, the polarization fraction has a unique azimuthal variation: higher along the major axis than the minor axis in the gaps, but vice versa in the rings. We find a rapidly declining polarization spectrum (with $p \propto \lambda^{-3}$ approximately) in the gaps, which becomes flattened or even inverted towards short wavelengths in the optically thick rings. These contrasting behaviours in the rings and gaps provide further tests for scattering-induced polarization via resolved multiwavelength observations.

Key words: polarization – protoplanetary discs – circumstellar matter.

1 INTRODUCTION

(Sub)millimetre polarization observations of discs around young stellar objects have been increasing in number, spatial resolution, and wavelength coverage (e.g. Rao et al. 2014; Stephens et al. 2014; Cox et al. 2015; Kataoka et al. 2016b; Fernández-López et al. 2016; Stephens et al. 2017; Alves et al. 2018; Bacciotti et al. 2018; Harris et al. 2018; Hull et al. 2018; Lee et al. 2018; Girart et al. 2018; Sadavoy et al. 2018a,b, 2019; Dent et al. 2019; Harrison et al. 2019; Mori et al. 2019; Vlemmings et al. 2019). The original scientific goal was to determine the magnetic field in discs through magnetically aligned grains, analogous to the interpretations of large-scale star-forming regions (e.g. Girart, Rao & Marrone 2006; Stephens et al. 2013; Hull et al. 2014). The magnetic fields are widely believed to play a key role in disc structure and dynamics (e.g. Blandford & Payne 1982; Balbus & Hawley 1991; Turner et al. 2014) that determine the conditions of planet formation (e.g. Morbidelli & Raymond 2016).

However, the theoretical interpretations of polarization observations of discs remain uncertain. In addition to alignment with the magnetic field via radiative torques (e.g. Andersson, Lazarian & Vaillancourt 2015), there are several other mechanisms that can align non-spherical grains, such as through radiative anisotropy (Lazarian & Hoang 2007a; Tazaki, Lazarian & Nomura 2017), mechanical alignment torques (Lazarian & Hoang 2007b; Kataoka, Okuzumi & Tazaki 2019), or aerodynamic alignment (Gold 1952;

★ E-mail: zdl3gk@virginia.edu
† NAOJ Fellow.

Lazarian 1995). Furthermore, the temperature structure may influence the interpretation of the alignment direction when discs are optically thick (Yang et al. 2017; Ko et al. 2020; Lin et al. 2020) and so does the porosity of non-spherical grains as long as the grain size is larger or comparable to wavelength (Kirchschlager, Bertrang & Flock 2019). To further complicate the situation, spherical grains can also produce polarization by dust self-scattering (Kataoka et al. 2015; Yang et al. 2016, 2017). Polarization by self-scattering depends on the radiation field of the observing wavelength. For inclined axisymmetric discs, the observational features can be simple: the polarization orientation tends to be along the disc minor axis; the level of polarization is roughly ~ 1 per cent; and the level of polarization is generally expected to decrease with increasing wavelength in the limit of scattering by grains smaller than the observing wavelength in an optically thin medium. Indeed, the scattering interpretation of disc polarization is favoured in several targets (e.g. Stephens et al. 2014; Cox et al. 2015; Kataoka et al. 2016b; Stephens et al. 2017; Bacciotti et al. 2018; Hull et al. 2018; Lee et al. 2018; Girart et al. 2018; Harris et al. 2018; Dent et al. 2019). However, given the plethora of polarization mechanisms, the scattering interpretation may not be unique. Independent evidence for dust scattering is highly desirable to validate the interpretation.

One way to validate scattering at (sub)millimetre wavelengths is through the dust continuum spectral index, α, defined by $\alpha \equiv \mathrm{d}\log I_\nu/\mathrm{d}\log \nu$, where I_ν is the intensity. Consider an isothermal slab of purely emitting dust (without scattering) with an optical depth of τ. In the Rayleigh–Jeans and optically thin ($\tau \to 0$) limit, $\alpha = \beta_{\rm dust} + 2$ where $\beta_{\rm dust}$ is the dust opacity index, defined by $\kappa_{\rm abs} \propto \nu^{\beta_{\rm dust}}$. $\kappa_{\rm abs}$ is the dust absorption opacity. It is expected that $0 < \beta_{\rm dust} \lesssim 2$ depending on the composition or size of the grain (e.g. Draine 2006). In the optically thick limit ($\tau \to \infty$), $\alpha = 2$, which is the frequency dependence of the Rayleigh–Jeans law, and the information of $\beta_{\rm dust}$ is lost. From an observational standpoint, it is convenient to define an inferred opacity index by $\beta \equiv \alpha - 2$. In this case, $\beta = \beta_{\rm dust}$ only in the optically thin limit ($\tau \to 0$) and $\beta = 0$ in the optically thick limit ($\tau \to \infty$). When scattering is included, Birnstiel et al. (2018) demonstrated that an increase in the albedo of grains decreases the emerging intensity, i.e. scattering makes objects appear dimmer. Zhu et al. (2019) further investigated the wavelength dependence of the one-dimensional (1D) scattering slab and deduced that, in the optically thin limit, $\alpha = \beta_{\rm dust} + 2$, which is the same relation as that without scattering. The difference is in the optically thick limit, where the albedo determines the spectral index: spectral index can be lower than 2 for an albedo that decreases with increasing wavelength. Liu (2019) demonstrated that the low spectral index of TW Hya can be explained by grains with maximum sizes on the order of 10–100 μm when scattering is included. This maximum grain size is on the scale of the grains inferred from polarization of other targets such as HD 142527 (Kataoka et al. 2016b), HL Tau (Kataoka et al. 2016a), and IM Lup (Hull et al. 2018). If scattering is the favoured mechanism for the polarization and the spectral index can in principle be explained by scattering, it is natural to ask: can scattering simultaneously reproduce both the polarization fraction and the spectral index in a particular object quantitatively? If so, the case for scattering would be greatly strengthened.

We seek to address the above question for the well-studied disc of the Herbig Ae star HD 163296. It is a Class II source at a distance of 101 pc (Gaia Collaboration et al. 2018). Rings and gaps in the disc were first resolved in Isella et al. (2016), using the Atacama Large Millimetre/submillimetre Array (ALMA) and further substructures were resolved in the Disc Substructures at High Angular Resolution Project (DSHARP; Andrews et al. 2018; Isella et al. 2018). The disc is a particularly suitable source to study polarization and the spectral index, since both measurements are available (Dent et al. 2019). It was shown in Dent et al. (2019) that the spatially resolved polarization image can be explained by dust self-scattering (see also Ohashi & Kataoka 2019). In particular, the polarization orientation is mainly along the disc minor axis and the anticorrelation of polarization fraction to the total intensity (Stokes *I*) of the dust emission along the major axis is broadly consistent with the expected anisotropy of the radiation field that plays an important role in the scattering-induced polarization (Kataoka et al. 2015; Yang et al. 2016). However, the model first explored in Dent et al. (2019) did not reproduce the low spectral index even though scattering was included. In particular, the central region of the disc, within a radius of ~40 au, has $\alpha < 2$ (i.e. $\beta < 0$). The unique combination of polarization pattern and low spectral index of HD 163296 provides a rare opportunity to quantitatively test whether dust scattering can reproduce both effects.

The structure of the paper is as follows: we prescribe a disc model in Section 2 and calculate the expected images based on a Monte Carlo radiative transfer code. The results are presented in Section 3. We discuss the results in Section 4 and conclude in Section 5.

2 MODEL SET-UP

In this section, we describe the dust opacity model and disc model considered to study HD 163926. To compare with observations, we will use the Monte Carlo radiative transfer code RADMC-3D[1] to produce observable quantities including polarization. The independent observational constraints considered are the high-angular resolution observations at Band 6 ($\lambda = 1.25$ mm) from DSHARP[2] (Andrews et al. 2018; Huang et al. 2018; Isella et al. 2018) with a synthesized beam full width at half-maximum (FWHM) of 0.038 arcsec × 0.048 arcsec, the polarization fraction at Band 7 ($\lambda = 0.87$ mm) with an FWHM of 0.21 arcsec × 0.19 arcsec, and the spectral index with an FWHM of 0.18 arcsec × 0.17 arcsec presented in Dent et al. (2019).

2.1 Dust opacity

We follow the DSHARP dust model prescribed in Birnstiel et al. (2018). Opacity is calculated using Mie Theory that assumes compact (non-porous) spherical grains and requires as input parameters the grain size and refractive indices. The dust model is a mixture of water ice, astronomical silicates, troilite, and refractory organic material with mass fractions of ~0.2, 0.33, 0.07, and 0.4, respectively. The respective refractive indices of the different components are taken from Warren & Brandt (2008), Draine (2003), and, for the latter two, Henning & Stognienko (1996). Furthermore, we average over a grain-size distribution that follows a simple power law, $a^{-3.5}$, with minimum and maximum grain-size cut-offs (the standard MRN grain-size distribution; Mathis, Rumpl & Nordsieck 1977), where a is the grain size. The minimum grain size is fixed at 0.01 μm, while the maximum grain size $a_{\rm max}$ is left as a free parameter. The precise value for the minimum grain size makes little difference at the considered wavelengths (Kataoka et al. 2015; Birnstiel et al. 2018). Mie opacity calculation is implemented using the PYTHON version of the MIE code available in RADMC-3D. The

[1] http://www.ita.uni-heidelberg.de/~dullemond/software/radmc-3d/
[2] https://bulk.cv.nrao.edu/almadata/lp/DSHARP/

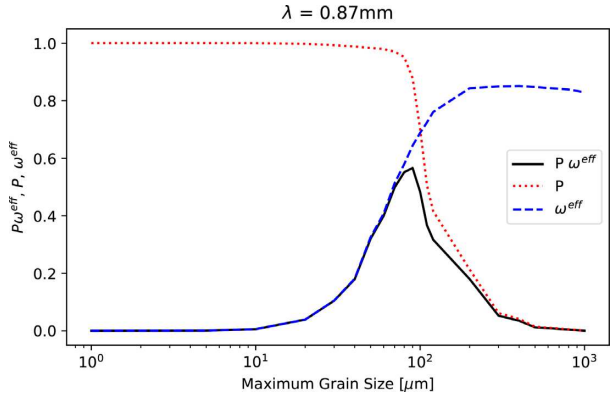

Figure 1. The calculated degree of linear polarization for single scattering (P; red dotted line), effective albedo discussed in Section 2.1 ($\omega^{\rm eff}$; blue dashed line), and the product $P\omega^{\rm eff}$ (black solid line) at $\lambda = 0.87$ mm for various grain sizes.

MIE code was ported from the FORTRAN 77 version by Bruce Draine[3] that is based on the original code published by Bohren & Huffman (1983).

A useful quantity to assess the dust scattering-produced polarization at a given wavelength, λ, is the product of the single scattering albedo, ω_ν, and single scattering polarization fraction taken at 90°, $P = -z_{12}/z_{11}$, where z_{12} and z_{11} are elements of the scattering matrix (Kataoka et al. 2015). ω_ν increases rapidly as the grain-size parameter $x \equiv 2\pi a/\lambda$ approaches unity, but P drops quickly for large ($x > 1$) grains. These two competing effects mean that the polarization at a given wavelength is determined by grains of a certain range of sizes (Kataoka et al. 2015). For a particle with a size larger than the wavelength, forward scattering dominates ω_ν even though forward scattering is effectively not scattering. A simple replacement for the apparent scattering efficiency is the effective albedo, $\omega_\nu^{\rm eff} = (1 - g_\nu)\omega_\nu$, where g_ν is the forward-scattering parameter (Ishimaru 1978; Birnstiel et al. 2018; Tazaki et al. 2019; Zhu et al. 2019). Fig. 1 shows the calculated P and $\omega_{\rm eff}$ for ALMA Band 7 ($\lambda = 0.87$ mm) as a function of the maximum grain size. The product, $P\omega_\nu^{\rm eff}$, gives the grain size that contributes most to the polarization at the observing wavelength. Fig. 1 shows that the optimal maximum grain size for producing polarization at $\lambda = 0.87$ mm is 90 μm. We will therefore hold $a_{\rm max}$ fixed at this value for our models and assume the same dust population throughout the whole disc; note that this value is somewhat smaller than the fiducial grain size of 140 μm adopted by Ohashi & Kataoka (2019) for their independent modelling of the HD 163296 disc polarization. The corresponding absorption opacity, effective albedo, and the forward-scattering parameter are $\kappa_{\rm abs} = 0.97$ cm^2 g^{-1} per gram of dust, $\omega_\nu^{\rm eff} = 0.64$, and $g_\nu = 0.15$ at $\lambda = 0.87$ mm, whereas at $\lambda = 1.25$ mm, $\kappa_{\rm abs} = 0.46$ cm^2 g^{-1}, $\omega_\nu^{\rm eff} = 0.47$, and $g_\nu = 0.044$. The opacity index $\beta_{\rm dust}$ index between the two wavelengths is 2.06.

2.2 Disc model

We consider a dust density distribution that is determined by distributions of surface density and scale height. We follow the DSHARP notation in Huang et al. (2018) to describe the substructures of HD 163296. For example, 'B100' represents the bright annular feature with a radius of 100 au. To model HD 163296-like discs with prominent substructures (rings and gaps), we adopt a composite surface density distribution Σ_d that is composed of two different types of profiles: power-law-like profiles and Gaussian-like profiles. The former consists of a power-law distribution within a region between radii of R_a and R_b and an exponential decrease interior and exterior to the region:

$$\Sigma_p(R) = \Sigma_{p,0} \times \begin{cases} \exp\left[-\frac{1}{2}\left(\frac{R-R_a}{\sigma_a}\right)^2\right], R < R_a \\ \left(\frac{R}{R_a}\right)^{-p}, R_a \le R < R_b, \\ \left(\frac{R_b}{R_a}\right)^{-p} \exp\left[-\frac{1}{2}\left(\frac{R-R_b}{\sigma_b}\right)^2\right], R \ge R_b \end{cases} \quad (1)$$

where R is the cylindrical radius, $\Sigma_{p,0}$ is the surface density at the inner edge R_a of the range, and p is the power-law index. The quantities σ_a and σ_b correspond to the characteristic distance over which the surface density decreases interior to R_a and exterior to R_b, respectively. This type of profile is particularly suitable for modelling the inner disc ($R < 50$ au) and the outer B100 region of HD 163296. Since gaps may not be entirely free of material, we adopt a surface density floor using the same power-law-like profile but with $p = 0$. We do not consider the innermost ring (B14) and gap (D10), because those features are not resolved in the spectral index map or in the polarization image that we seek to model. We also ignore the small-scale non-axisymmetric (crescent-like) feature interior to B67 for simplicity.

The Gaussian-like profile is prescribed as

$$\Sigma_G(R) = \Sigma_{G,0} \times \begin{cases} \exp\left[-\frac{1}{2}\left(\frac{R-R_0}{\sigma_c}\right)^2\right] & , R \le R_0 \\ \exp\left[-\frac{1}{2}\left(\frac{R-R_0}{\sigma_d}\right)^2\right] & , R > R_0 \end{cases}, \quad (2)$$

where R_0 is the radius of the centre of the profile, $\Sigma_{G,0}$ is the surface density at R_0, and σ_c and σ_d are the widths of the Gaussian distributions interior and exterior to R_0, respectively. This type of profile is particularly suited for modelling rings. The full surface density profile is obtained by summing all the various power-law-like and Gaussian-like profiles:

$$\Sigma_d = \sum_i \left(\Sigma_p\right)_i + \sum_i \left(\Sigma_G\right)_i, \quad (3)$$

where i is the dummy variable that iterates through the number of assigned components.

For the temperature distribution of the large (90 μm) grains that are responsible for the scattering-induced polarization in our model, we adopt the following simple power law:

$$T = T_t \left(\frac{R}{R_t}\right)^{-q}, \quad (4)$$

where T_t is the temperature at a characteristic radius R_t and q is the power-law index.[4] For our Monte Carlo radiative transfer calculations of the disc polarization and spectral index, the mass

[3] https://www.astro.princeton.edu/~draine/scattering.html

[4] We refrain from introducing additional parameters to characterize the vertical variation of the temperature of the dust, because, as we show later, the scale height of the approximately 0.1 mm-sized grains in our model is significantly smaller than that of the gas, which should make the temperature in the relatively thin dust layer similar to that of the mid-plane for a passive disc.

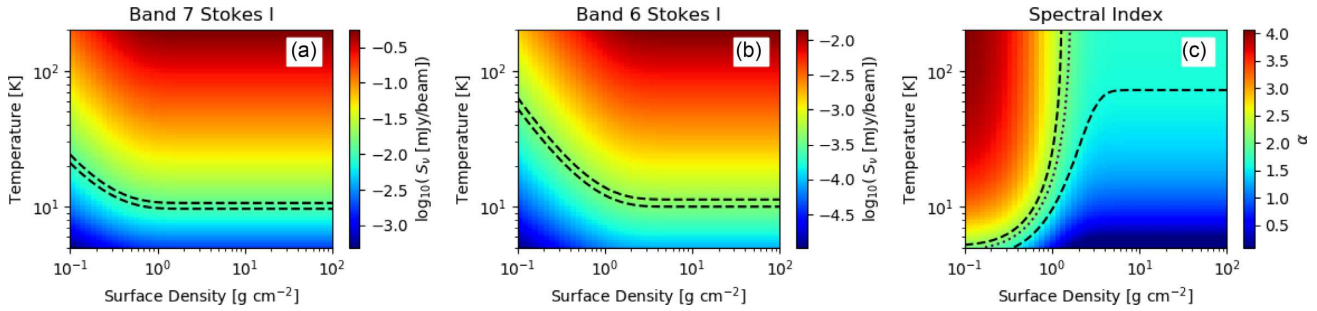

Figure 2. The plane–parallel calculation of an isothermal scattering slab in the two-dimensional parameter space of surface density and temperature. The panels from the left to right are Band 7 Stokes *I*, Band 6 Stokes *I*, and spectral index between the two ALMA bands. The dashed lines bracket the observed range for ring B100 of HD 163296. The dotted line in panel (c) marks where $\alpha = 2$.

density of the dust must be specified. It is parametrized by

$$\rho(R, z) = \frac{\Sigma_d(R)}{\sqrt{2\pi}H} \exp\left[-\frac{1}{2}\left(\frac{z}{H}\right)^2\right], \quad (5)$$

where z is the cylindrical height and H is the dust scale height, parametrized as $H = H_t(R/R_t)^{q/2+3/2}$. Ideally, both the dust and temperature distributions should be computed self-consistently, but doing so is numerically costly and it would require additional assumptions about the level of turbulence in the disc and the abundance of small grains that absorb the stellar radiation near the disc surface. These are beyond the scope of this paper.

2.3 Using the 1D slab model to estimate parameters

To constrain model parameters, one can implement a grid-based search or other parameter fitting methods, e.g. Markov Chain Monte Carlo. However, polarization radiative transfer calculations are computationally expensive; thus, we choose to first estimate the parameters needed to fit the Bands 6 and 7 data observed in HD 163296 at several representative locations with the help of a 1D (plane-parallel) analytic model.

Following Birnstiel et al. (2018) and Zhu et al. (2019), we consider a 1D isothermal slab with scattering where the observed intensity at a given wavelength can be computed analytically for different optical depths and temperatures. We fix the inclination angle to 46.7°, which was measured by fitting ellipses to the continuum annular substructures (Isella et al. 2018). Using the opacity determined in Section 2.1, we search through a parameter space of temperature and surface density of the slab and calculate the expected intensities at ALMA Bands 6 and 7 and the spectral index between the two.

The colour maps of Fig. 2 show the calculated intensity at Bands 7 and 6 and the spectral index. The intensities are scaled by the respective finite beam sizes of the observations for direct comparison in the remainder of this section. For a given temperature, the intensity increases with increasing surface density and reaches an asymptotic value as the slab becomes optically thick (see equation 12 of Zhu et al. 2019) as seen in Figs 2(a) and (b). From Fig. 2(c), we see that the spectral index in the optically thin limit measures the opacity index determined by the absorption opacity and decreases to a constant value determined by the albedo and viewing inclination as the optical depth increases (see equations 21 and 22 of Zhu et al. 2019). The constant value in the optically thick regions can have $\alpha < 2$, i.e. $\beta < 0$ (the right-hand side of the dotted line in Fig. 2c). We can also see that at low temperatures where the Rayleigh–Jeans limit is inapplicable, the spectral index decreases faster and also reaches a lower value. This is because the Planck function produces lower intensity at higher frequency than that in the Rayleigh–Jeans limit and thus creates a lower spectral index.

We directly compare with the observations using the values at B100 as a demonstration in Fig. 2. We overlay the range that encloses 10 per cent of the measured Stokes *I* at Bands 7 and 6 to account for the absolute flux calibration uncertainty of ALMA observations and an uncertainty of 0.3 for the measured spectral index (Dent et al. 2019; which used a 7 per cent calibration uncertainty). There is a limited range of surface density and temperature that can simultaneously reproduce the data. These constrained ranges serve as a consistency check and provide a starting point for exploring the parameter space using Monte Carlo radiation transfer calculations in Section 3.

In Fig. 3, we overplot the regions that fulfill the observed constraints within its uncertainty for the three representative radii of the bright bands: 20, 67, and 100 au. The constraints are listed in Table 1. In Fig. 3(a), there is a threshold surface density above which increased surface density does not alter the intensity and spectral index. This threshold is achieved simply because both wavelengths become optically thick, thus the intensity only depends on wavelength or temperature. At B67, or panel 3(b), there is only a limited range of surface densities suggesting that the ring cannot be optically thin or very optically thick (unlike the inner disc). For both panels 3(b) and (c), the intersecting range is in the region where spectral index falls quickly with surface density, which hints that these rings are not in the Rayleigh–Jeans limits.

3 NUMERICAL RESULTS

3.1 Polarization image

Guided by the analytical estimates in Section 2.3, we performed a set of RADMC-3D-based radiative transfer calculations including polarization from scattering. A chosen set of parameters for the model that fits the observational data for HD 163296 is presented in Table 2. We plot the image results in Fig. 4. To consider finite resolution, the Stokes *I* images are convolved by a Gaussian beam with a circular FWHM of 0.043 arcsec for Band 6. The polarized intensity, polarization fraction, and polarization orientation at Band 7 are produced after the Stokes *Q* and *U* images are first convolved individually with a circular FWHM of 0.2 arcsec. The spectral index is calculated after Band 7 and 6 Stokes *I* are each convolved by a Gaussian beam with a circular FWHM of 0.175 arcsec first to match that from Dent et al. (2019). The values for the FWHM are

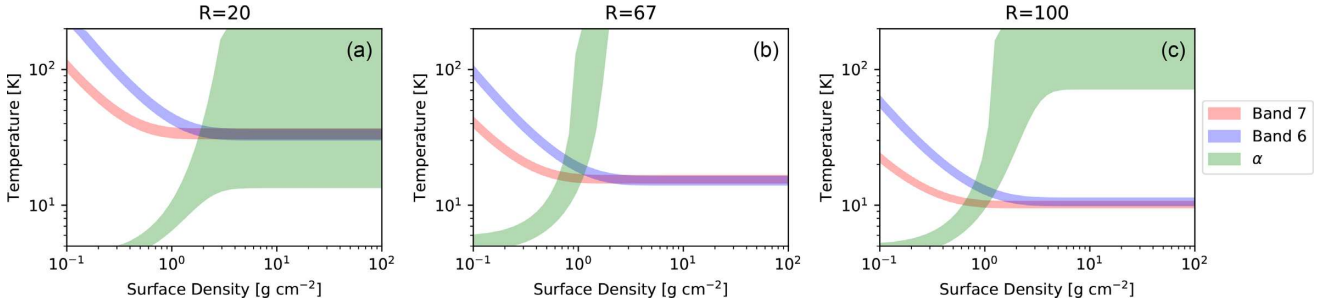

Figure 3. The range of surface density and temperature constrained by observations at 20, 67, and 100 au. The red, blue, and green regions correspond to ranges constrained by the Band 7 Stokes *I*, the Band 6 Stokes *I*, and the spectral index between Bands 7 and 6.

Table 1. Values from observations used for 1D slab estimation in Section 2.3. The first column is the radius in au. The second to fourth columns are the observed values for the fluxes in Bands 7 and 6 and the spectral index α between the two bands.

Radius (au)	Band 7 (mJy beam^{-1})	Band 6 (mJy beam^{-1})	α
20	78.1	2.08	1.4
67	26.2	0.76	2.2
100	12.0	0.44	1.9

the geometric mean of the major and minor axes of the respective synthesized beams.[5] The images are only plotted up to 125 au in radius because we are mainly interested in the region with detected polarization (Dent et al. 2019).

One can quickly verify that the Stoke *I* of Band 6 is qualitatively similar to the observations. The inner disc and the rings produce higher intensity relative to the gaps. Furthermore, the general polarization features at Band 7 match those of the observations. The polarized intensity is larger in the inner disc and rings. The polarization orientations are mainly in the disc minor axis direction, within $\sim\pm10^\circ$ across the image. We plot the deviation, $\Delta\theta$, from the disc minor axis ($x = 0$) in panel (e) of Fig. 4 in order to show the variation of polarization orientation.

The distribution of polarization orientation is similar to that observed and modelled by Dent et al. (2019) and Ohashi & Kataoka (2019). The polarization orientation is largely along the disc minor axis, which is expected for a disc (Yang et al. 2016, 2017). The distribution of the deviation reflects the radiation anisotropy previously discussed in Kataoka et al. (2015), Yang et al. (2016), and Yang et al. (2017). For example, in an optically thin gap, most of the radiation comes from the adjacent rings or the inner disc, which is in the radial direction. The radial radiation anisotropy leads to a slightly more azimuthal polarization orientation in the gaps, as observed (see fig. 1d of Dent et al. 2019).

3.2 Profiles along the major axis

For more quantitative comparisons, we take a cut along the major axis and compare the beam-convolved model images to observations in panels (a)–(c) of Fig. 5 that show, respectively, the Stokes *I* of Band 6, the polarization fraction in Band 7, and the spectral index between Bands 7 and 6. The polarization data are taken from fig. 2(a) of Dent et al. (2019), where the polarization along the major axis is separated into the northwest and southeast directions. Note that the low spectral index values of $\sim$1.5 and the polarization fraction of $\sim$ 1 per cent in the inner disc are well reproduced. The model optical depths along the major axis at Bands 7 and 6 are plotted in panel (d).

To identify the effects of convolution, we also plot the intrinsic model images without convolution. In the gap regions, the intrinsic spectral index approaches $\alpha \sim 4$, which is expected since the grains we are using have $\beta_{\rm dust} = 2.06$ (recall in the Rayleigh Jeans limit, $\alpha = \beta_{\rm dust} + 2$). In the optically thick rings, the spectral indices are intrinsically low ($\sim$1.5) because of preferential scattering at shorter wavelengths, although deviation of the blackbody radiation from the Rayleigh–Jeans limit also plays a role, especially for the outer, colder ring. The observed rings have $\alpha \sim 2$, which is not as low as that in the inner disc since the emission from the rings is blended with emission from the gaps that have much higher spectral indices.

The polarization fraction after convolution coincides with the observed polarization within the first gap, but is somewhat lower than the observed values at outer radii given by Dent et al. (2019). However, our model matches better the polarization fraction presented in Ohashi & Kataoka (2019) at outer radii (see e.g. the top panel of their fig. 18). We should caution the reader that the polarization fraction may be significantly affected by the differential filtering of Stokes *I* versus *Q* and *U* by interferometers such as ALMA. This effect has yet to be thoroughly quantified, and will be explored elsewhere.

4 DISCUSSION

4.1 Consistency check and discrepancies

4.1.1 Optical depth

We find that a grain size of 90 μm, similar to the 100 μm found in Dent et al. (2019), reproduces their observed level of polarization in the inner disc, although it is lower beyond the first gap. However, the spectral index they obtained was $\sim$3.5 even in the inner disc and rings, which is most likely due to a lower optical depth adopted in their model compared with ours. For the inner disc at radius $R \lesssim$ 30 au, we find that optical depths of $\sim$10 at Band 6 and higher for Band 7 are needed to produce the low spectral index observed there. The high optical depth of the inner disc implies that one would not be able to see the line emission from the back side of the disc (Zhu et al. 2019). This seems to be the case judging from the DSHARP

[5]We use only circular FWHM beams for simplicity; nevertheless, the major and minor axes of the spectral index map are very similar. The Band 6 DSHARP beam is more elliptical, although the precise beam shape should be important only for the small structures which were not resolved in Band 7. We have checked that using the elliptical beam size for the Band 6 DSHARP data does not significantly modify the results.

Table 2. A chosen set of parameters for the model. The first column displays the name of the parameter from Section 2 and its corresponding units in squared brackets. The parameters are separated into three main groups: the general parameters, parameters used for power-law-like surface density components, and parameters used for Gaussian-like surface density components. For the inner disc, the inner exponential decrease is ignored since it is not resolved and thus $\sigma_a = 0$.

Parameters				
R_t (au)	100			
T_t (K)	12.5			
q	0.65			
H_t (au)	3			
B2				
Power-law-like surface density				
Feature	Inner Disc	D48	D86	B100
$\Sigma_{p,0}$ (g cm^{-2})	8	0.02	0.1	0.5
p	0	0	0	7
R_a (au)	0.5	38	76	105
R_b (au)	26	58	96	135
σ_a (au)	0	5	5	5
σ_b (au)	6	4.5	5	10
B2				
Gaussian-like surface density				
Feature	B67	B100	B155	
$\Sigma_{G,0}$ (g cm^{-2})	2.5	2.1	0.15	
R_0 (au)	67	100	155	
σ_c (au)	5	3	5	
σ_d (au)	5	4	25	

^{12}CO channel maps (Isella et al. 2018); however, confirmation of this claim is beyond the scope of this paper. For the dust rings at 67 and 100 au, we find optical depths of ∼3 at their centres in Band 6. These values are consistent with the constraints provided by Isella et al. (2018), who found lower limits of ∼0.6 and 0.7, respectively, based the level of extinction of the ^{12}CO emission from the back side of the disc.

4.1.2 *Temperature*

In Fig. 5(e), we compare the brightness temperature at Band 6 and the input temperature profile as a function of radius. Our temperature determination is based on the spectral index between Bands 6 and 7 and on the Band 7 polarization data. It is particularly driven by the temperature at the outer, 100 au ring. The fact that this ring has a spectral index α close to 2 (see the last column of Table 2 and Fig. 5b) indicates that it is most likely optically thick (this is discussed further in Appendix A), unless the grains responsible for most of its emission are much larger than the observing wavelengths. However, such large grains would not scatter the photons at the observing wavelengths efficiently and would have difficulty reproducing the observed polarization (Kataoka et al. 2015; Yang et al. 2016). If the outer ring is indeed optically thick, its temperature would naturally be close to the relatively low brightness temperature that we observe (shown in Fig. 5b as shaded line), which is indeed what we find from our modelling; the small difference between the two is attributed to scattering (Birnstiel et al. 2018). We therefore believe that, broadly speaking, our mid-plane dust temperature makes physical sense.

In Fig. 5(e), we further plot the mid-plane temperature profiles found from existing literature based on CO lines, but scaled to our adopted distance of 101 pc: $19(R/128\ \mathrm{au})^{-0.3}$ K (Rosenfeld et al. 2013), $22.5(R/124\ \mathrm{au})^{-0.3}$ K (Flaherty et al. 2015), and $18.7(R/400\ \mathrm{au})^{-0.14}$ K for $R > 60$ au (Dullemond et al. 2020). We find that our mid-plane dust temperature is lower than these profiles. In particular, Dullemond et al. (2020) presented a clever way of inferring the gas temperature at the disc mid-plane based on the brightness temperature of optically thick CO lines at the

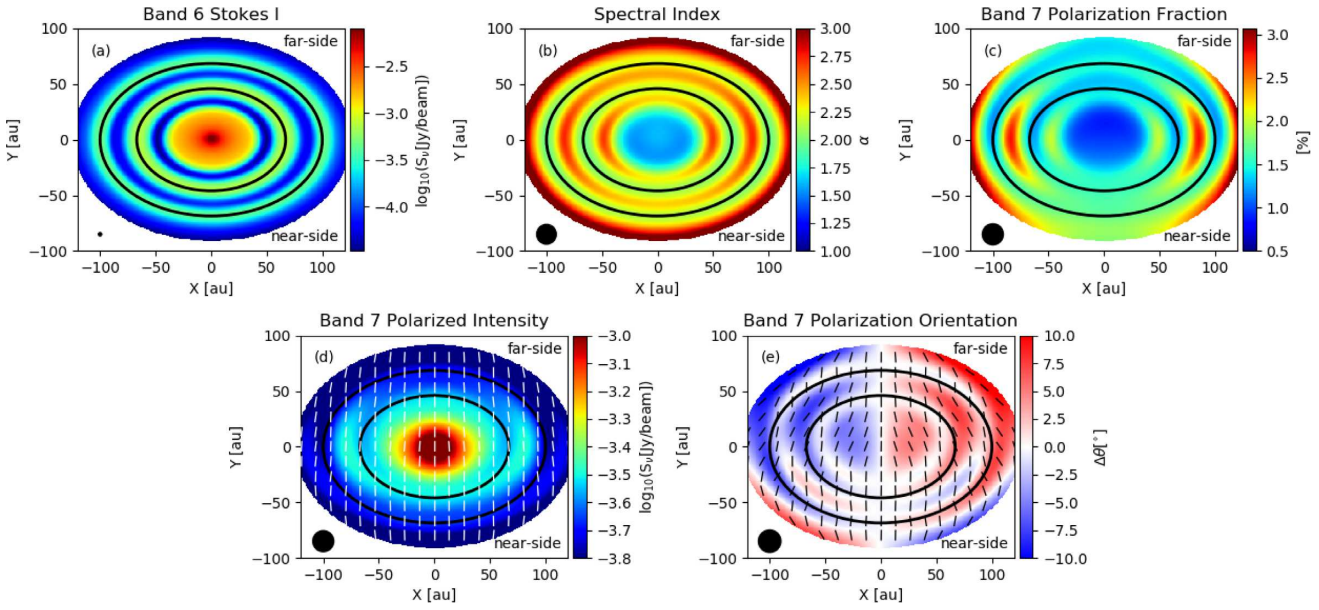

Figure 4. The two-dimensional images of the disc model. The near side of the disc is the bottom half of the image. Panel (a): The Band 6 Stokes *I* image in Jy beam^{-1}. Panel (b): The spectral index between Bands 7 and 6. Panel (c): The Band 7 polarization fraction in per cent. Panel (d): The Band 7 polarized intensity in Jy beam^{-1}, with the polarization vectors overplotted. Panel (e): The colour scale depicts the offset of the polarization orientation, $\Delta\theta$, from the vertical direction (parallel to the disc minor axis). $\Delta\theta$ is plotted east from north (counterclockwise) and $\Delta\theta = 0$ means the polarization orientation is parallel to the disc minor axis. The vectors in Panel (e) are oriented from the vertical direction by $3 \times \Delta\theta$ to make the offsets obvious. The black ellipses for all six panels denote the rings. The Gaussian beams used for convolution are plotted as black filled circles at the lower left.

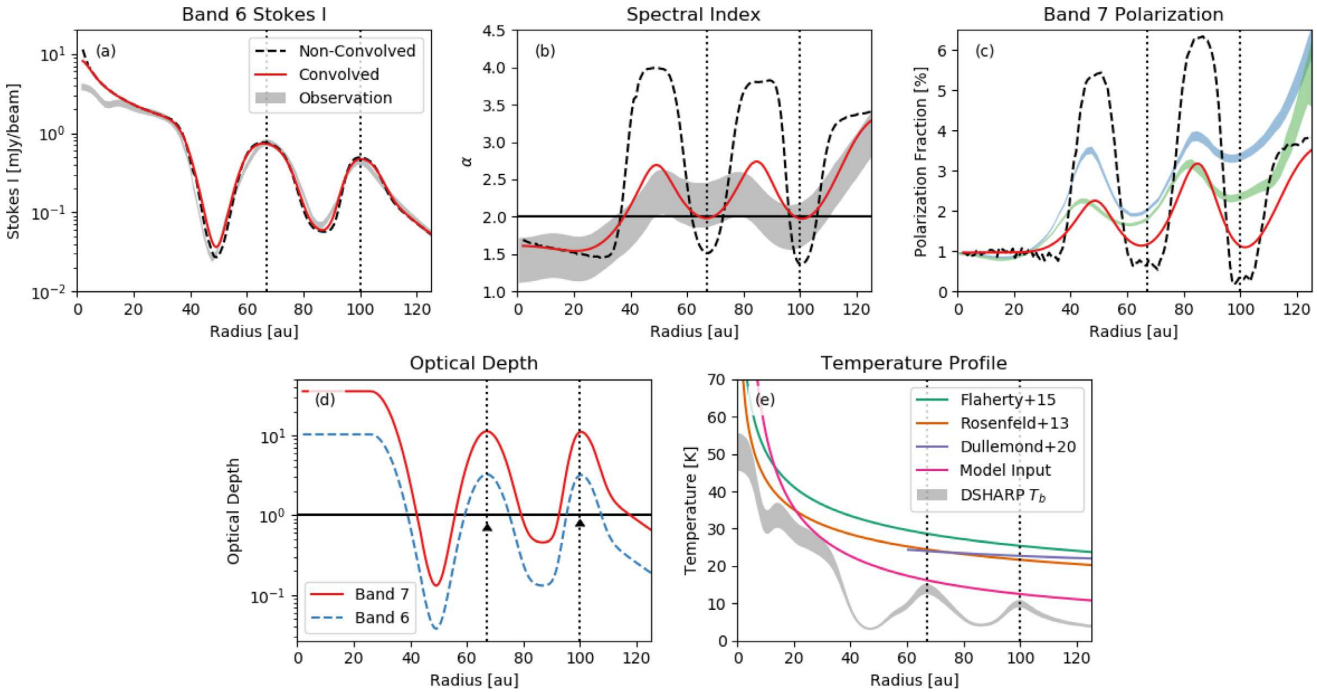

Figure 5. Panel (a): The 0.043 resolution Band 6 Stokes *I* image in mJy per beam. The units of the non-convolved image is scaled to the corresponding mJy per beam. The convolved profile is plotted with a red solid line, the non-convolved profile with a black dashed line, and the grey region represents the ± 10 per cent calibration uncertainty of the data. Panel (b): The spectral index between Bands 7 and 6. The grey region is $\alpha \pm 0.3$, where α is the spectral index averaged between the northwest and southeast major axes. The $\alpha = 2$ is plotted as a horizontal solid line. Panel (c): We plot the convolved Band 7 polarization with a red solid line and the non-convolved polarization with a black dashed line. The green and blue coloured regions are the observed Band 7 polarization with uncertainty from random noise and image fidelity along the northwest and southeast major axes of the disc (Dent et al. 2019). Panel (d): The model optical depth along the major axis for Bands 7 and 6. The lower limits for Band 6 optical depths at 67 and 100 au (denoted by triangles) are derived from the level of ^{12}CO extinction through the dust rings (Isella et al. 2018). The optical depth of 1 is plotted as a horizontal solid line. Panel (e): A comparison of various dust temperature profiles as a function of radius from previous literature. The vertical dotted lines through all the panels are the locations of the rings.

line-of-sight velocity expected of the mid-plane. As stressed by Dullemond et al. (2020), this method relies on the assumption that CO molecules are present at the mid-plane and are not frozen out on to dust grains. Their inferred gas temperature drops from ∼25 K at ∼100 au to ∼18 K at ∼400 au, although there are significant variations, especially near the 100 au ring, where $T \sim 20$ K. In the inner, ∼100 au region that is of direct interest to us, their inferred temperature is close to but above the CO freeze-out temperature. If optically thick CO is present at the mid-plane, the gas (and dust) temperature at the mid-plane would indeed be of order 20 K or more, which would be significantly higher than the dust temperature that we infer at the same radius. However, if the CO is frozen-out at the mid-plane, it would not probe the mid-plane temperature. It would probe, instead, the temperature of the so-called CO snow surface above (or below) the mid-plane where the warmer CO-rich gas transitions to the colder CO-poor gas (and dust). If the snow surface is spatially close enough to the mid-plane, it may not be easy to kinematically distinguish it from the mid-plane, especially in view of the fact that the CO lines are broadened by thermal motions, optical depth effects, and potentially some level of turbulence (Flaherty et al. 2015, 2017). While the results of Dullemond et al. (2020) by themselves are consistent with a relatively warm mid-plane temperature of 20 K or more on the 100 au scale, they do not exclude the possibility of a colder mid-plane that is out of the reach of their CO-based method because of CO freeze-out. Therefore, we conclude that our dust-based temperature does not necessarily contradict those CO-based temperature estimates from the literature, particularly that of Dullemond et al. (2020).

In fact, if the dust temperature at the mid-plane were as high as those inferred from optically thick CO lines, we would have difficulty reproducing the continuum data. This is illustrated in Appendix A, where we redid the model shown in Fig. 5 using a higher temperature profile from Flaherty et al. (2015). The higher temperature model does not fit the spectral index, especially at the outer, 100 au ring. As stated earlier, this is simply because the higher temperature model requires less dust (and thus a lower dust optical depth), but the ∼ 100 μm-sized grains needed for scattering-induced polarization cannot produce the observed flat spectral index of $\alpha \sim 2$ unless they are optically thick. This is strong evidence that the disc mid-plane is colder than the temperatures inferred from optically thick CO lines, which most likely probe the warmer gas from the disc surface down to the CO snow surface rather than the colder mid-plane region, as discussed above.

The Band 6 Stokes *I* for the innermost part of the disc ($\lesssim$10 au) appears to be higher than the observed value, indicating that the simple power-law temperature profile breaks down at small radii. The prescribed temperature profile also does not take into account the rings and gaps, which may be required for more precise fitting.

4.1.3 Dust scale height

In our model, the dust scale height is found to be 3 au at a radius of 100 au. For a disc with dust settling, the dust vertical distribution is balanced by the downward gravity and the upward turbulent mixing. This results in a height that is a fraction of the gas pressure scale

height (Dubrulle, Morfill & Sterzik 1995; Armitage 2015). For an estimation, we approximate the fraction by

$$\frac{H_{\rm d}}{H_{\rm g}} \sim \sqrt{\frac{\alpha_v}{\Omega\tau_{\rm f}}}, \tag{6}$$

where $H_{\rm d}$ is the dust scale height and $H_{\rm g}$ is the gas pressure scale height. The quantity α_v here is the viscosity parameter (not to be confused with the spectral index); Ω is the Keplerian orbital frequency; and $\tau_{\rm f}$ is the frictional time-scale defined by $\tau_f \equiv \rho_{\rm s} a/\rho_{\rm g} c_{\rm s}$ where $\rho_{\rm s}$ is the mass density of the solid, $\rho_{\rm g}$ is the gas density, and $c_{\rm s}$ is the thermal sound speed. We estimate the gas density structure from the multi-line fitting results in Flaherty et al. (2015) scaled to our adopted distance of 101 pc. At a radius of 100 au, $H_{\rm g} = 8.7$ au, gas surface density is 3.9 $\rm g\,cm^{-2}$ and $\rho_{\rm g} = 1.2 \times 10^{-14}\,\rm g\,cm^{-3}$. From Section 2.1, the grain size is 90 μm and $\rho_{\rm s} \sim 1.7\,\rm g\,cm^{-3}$. We use the temperature found in Section 3 for $c_{\rm s}$. Using our prescribed dust scale height, the $\alpha_v \sim 1.7 \times 10^{-3}$. The upper limit on the viscosity parameter was found to be $\alpha_v \lesssim 1 \times 10^{-3}$ (Flaherty et al. 2015) which is broadly consistent with our model result. Ohashi & Kataoka (2019) considered two different dust populations with different scale heights, $H_{\rm d}$, at different radii to fit the polarization and found that $H_{\rm d}/H_{\rm g} \lesssim 1/3$ for $R \lesssim 70$ au and $H_{\rm d}/H_{\rm g} \sim 2/3$ for $R \gtrsim 70$ au. Our results are consistent with the conclusion from Ohashi & Kataoka (2019) and using a larger dust scale height at larger radii may increase the polarization fraction for our model.

4.2 Apparent low opacity index from beam averaging of rings and gaps

Measurements of the spectral index at (sub)millimetre wavelengths have long been used to infer grain sizes in protoplanetary discs. In particular, a relatively low inferred opacity index $\beta \equiv \alpha - 2 \lesssim 1$ has often been taken as evidence for grains up to millimetre size or larger (Beckwith & Sargent 1991; Testi et al. 2014). Such large (mm) sizes are in tension with the grain sizes inferred from disc polarization if the polarization arises from dust scattering (Kataoka et al. 2015). For example, in the case of HL Tau, polarization suggested $\sim$ 100 μm grains (Yang et al. 2016; Kataoka et al. 2016a), while the apparently low opacity index is taken as evidence for millimetre grains (Carrasco-González et al. 2019, see below).

The same tension appears to exist for the target of the current study, HD 163296: namely, the Band 7 polarization is most naturally produced by 100 μm-sized grains through scattering but the apparent opacity index β is less than unity at small radii (within about 100 au; see Fig. 5b) which, in the usual interpretation, requires mm-sized grains. However, in this particular case, we have demonstrated that the low values of β can be produced by small, 100 μm-sized grains because of high-contrast disc substructures (specifically rings and gaps) *and* the averaging of the emission from these substructures. In particular, in our best-fitting model shown in Fig. 5(b), we have $\beta \sim 2$ in the optically thin gaps and $\beta \sim -0.5$ in the optically thick rings. The negative β comes from more efficient scattering at the shorter wavelength. After convolution with the telescope beam, the former is brought down to $\beta \sim 0.5$, and the latter up to $\beta \sim 0$. Therefore, in our interpretation, the low apparent opacity index β in the inner gaps of the HD 163296 disc does not correspond to $\beta_{\rm dust}$. As such, it cannot be used to infer the presence of large (mm-sized) grains. In this particular case, the tension in the estimation of grain size from polarization and opacity index $\beta_{\rm dust}$ may be illusory. An implication is that the grain growth may be stifled around a relatively small size of order 100 μm for some reason (e.g. coating of grains by relatively non-sticky CO_2 ice that makes it harder for the grains to grow through collisions, Okuzumi & Tazaki 2019). Another possibility is that there are indeed larger grains, although it may be hidden within the optically thick 100 μm grains.

Our modelling of the specific case of HD 163296 highlights the general need for caution in evaluating the spectral index in discs that have intrinsically high contrast substructures right next to one another, such as rings and gaps. This point was made by ALMA Partnership et al. (2015), among others, but it is worth stressing, particularly in the context of the aforementioned tension in two different methods of grain-size estimation. It is especially true when optically thin and optically thick substructures are located close together and the grains responsible for the emission are much smaller than the observing wavelengths. In such cases, there is rapid spatial variation of the spectral index from $\alpha \sim 4$ in the optically thin substructures to $\alpha \sim 2$ (or less if scattering is important and more efficient at a shorter wavelength) in the optically thick substructures. If the substructures are not (or are only barely) resolved observationally, their fluxes will be blended together, which will artificially increase the spectral index in the optically thick substructures and decrease that in the optically thin substructures. Because of their intrinsically low values, the fluxes in the optically thin substructures are especially susceptible to telescope beam averaging; the substructures must be well resolved in order to prevent the (high) fluxes from the optically thick substructures from leaking into the optically thin regions and overwhelming the (weak) intrinsic emission there. If there is significant contamination from the optically thick substructures, the optically thin regions will have a spectral index substantially lower than ∼4, which may be misinterpreted as evidence for large grains. Conversely, contamination from the optically thin substructures may change the spectral index in an optically thick region from $\alpha < 2$ to $\gtrsim 2$, thus potentially hiding evidence for strong scattering.

Given the wide-spread substructures detected in protoplanetary discs through DSHARP (Andrews et al. 2018) and other programmes, there is a need to re-evaluate whether the relatively low opacity index commonly inferred for discs in the literature (Testi et al. 2014), especially from early low-resolution observations (e.g. Beckwith & Sargent 1991), is significantly affected by beam averaging or not. If so, it would go a long way towards alleviating the tension between the grain sizes inferred from spectral index studies versus that from scattering-induced polarization studies. High-resolution observations that *well* resolve the disc substructures at multiple wavelengths are needed to determine whether the tension is real or merely a reflection of scattering and beam averaging.

4.3 Polarization spectrum as a test of scattering-induced polarization

Besides low ($\alpha \lesssim 2$) spectral index, an additional test of the scattering interpretation of the polarization detected in HD 163296 can come from multiwavelength data. In the optically thin gaps, the relatively small dust grains that we used in our models to maximize the polarization at ALMA Band 7 ($\lambda = 0.87$ mm) are expected to produce lower polarization fractions at longer wavelength bands, since the scattering should be in the Rayleigh regime where the scattering cross-section drops rapidly with increasing wavelength. If the inner disc and the first two rings are really optically thick, as indicated by our modelling, then the polarization spectrum (the distribution of the polarization fraction as a function of wavelength) would be different. In particular, Yang et al. (2017) showed that

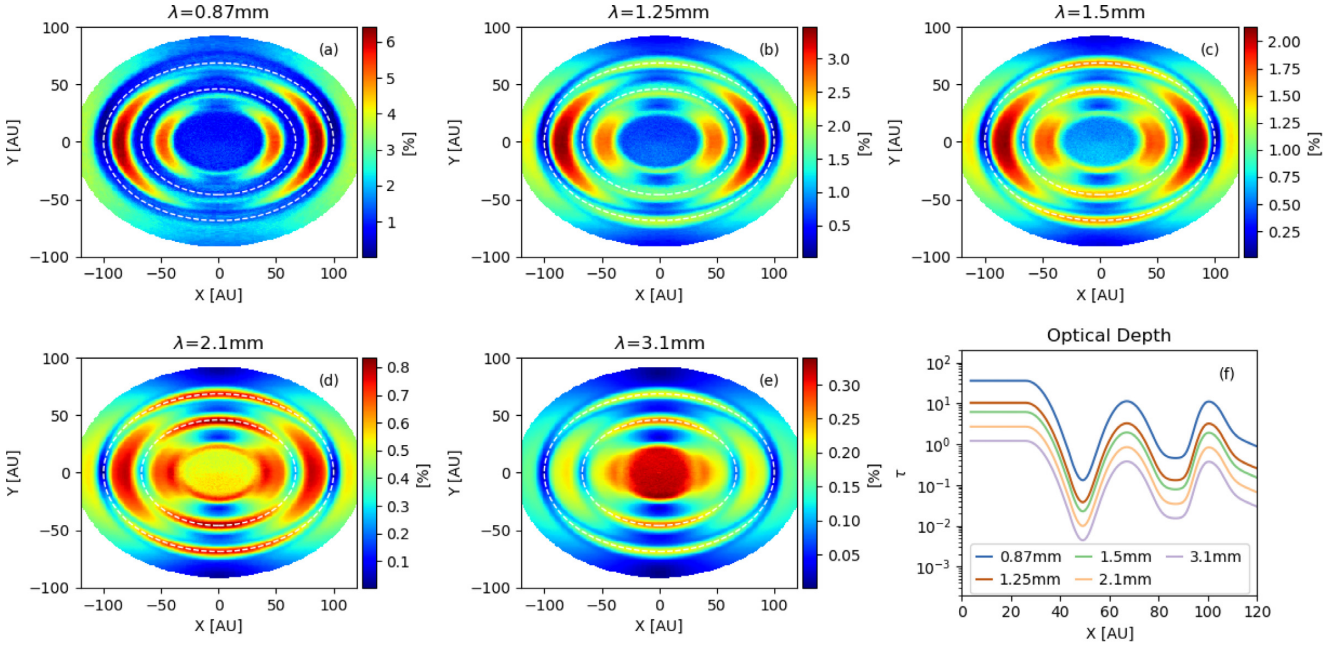

Figure 6. Images of the polarization fraction without finite telescope resolution for 5 ALMA bands at $\lambda = 0.87$, 1.25, 1.5, 2.1, and 3.1 mm (panels a–e), where the polarization capability is available. The dashed white ellipses mark the location of the rings. Panel (f) plots the distribution of the optical depth as a function of radius along the major axis for each band.

scattering-induced polarization fraction peaks around an optical depth of order unity for an inclined slab, dropping quickly to zero as the optical depth goes to zero and asymptoting to a finite value as the optical depth goes to infinity (see their fig. 3). It is unclear at the present time whether these expectations are met or not, since there is only polarization data at one Band (Band 7). Here, we will make predictions for all other bands where polarization observations are currently possible with ALMA, including Bands 6, 5, 4, and 3 (corresponding to λ =1.25, 1.5, 2.1, and 3.1 mm, respectively). These can be checked against future observations.

In Fig. 6, we plot the spatial distribution of the polarization fraction in each of the ALMA bands in colour scale (panels a–e) without effects of finite telescope spatial resolution. We also plot the radial distribution of the optical depth along the major axis for each band (panel f). Note that the maximum value for the colour scale is different for each band, starting at ~ 6 per cent for the shortest wavelength Band 7 and decreasing to ~ 0.35 per cent for the longest wavelength Band 3. The change of polarization fraction with wavelength is discussed in detail below. Here, we focus on the spatial distribution of the polarization fraction, which has an interesting transition from Band 7 to Band 3. For all images, the azimuthal variation along the rings versus that along the gaps are opposite. Along the rings, the polarization fraction is higher along the minor axis ($x = 0$). Along the gaps, the polarization fraction is higher along the major axis ($y = 0$). The former trend is most clearly seen in the Band 3 image, while the latter trend is most obvious at Band 7.

The azimuthal variation can be understood in terms of two competing effects: the inclination-induced polarization and the radiation-anisotropy-induced polarization. For both the rings and gaps, the inclination-induced polarization produces polarization parallel to the disc minor axis, but the radiation anisotropy is different between the rings and gaps. The radiation in the gaps comes mostly from the adjacent rings (or the inner disc), with an anisotropy in the radial direction leading to an azimuthally oriented polarization that adds to the inclination-induced polarization at locations along the disc major axis, but offsets the polarization at locations along the minor axis. On the other hand, the radiation in the rings comes mostly from the azimuthal direction, leading to a radially oriented polarization that offsets the inclination-induced polarization at locations along the major axis, but adds to the polarization at locations along the minor axis (see also Pohl et al. 2016, their fig. 7). Such azimuthal variations for rings and gaps are present at the same time for Band 4 (panel c) and Band 5 (panel d).

Another interesting trend is that, as the wavelength increases, the inner disc becomes more prominent in the polarization fraction map: compared with the rings and gaps at large radii, its polarization fraction is lower at Band 7, but becomes higher at Band 3. The former is due to high optical depth (see panel f), while the latter comes about because the inner disc has an optical depth of order unity at Band 3, which is optimal for producing polarization through scattering (Yang et al. 2017). In all cases, the polarization orientations are broadly similar to that displayed in Fig. 4(e) for Band 7, with the deviation angles from the disc minor axis increasing somewhat with wavelength.

In Fig. 7, the predicted polarization spectra (polarization fraction as a function of wavelength) are plotted for three representative locations on the major axis: the inner disc at $R = 20$ au, the D48 gap, and the B67 ring. In the gap, the polarization fraction decreases monotonically with increasing wavelength and approaches the steep power-law λ^{-3} for Rayleigh scattering towards the longest wavelength bands with the lowest optical depths. In the ring, the spectrum is drastically different. The polarization fraction is higher for the longer wavelength Band 6 than the shorter wavelength Band 7, which is the opposite of the common expectation based on the simplest Rayleigh scattering. The reason for this spectral inversion is that the ring is optically thick at both wavebands, but more so at the shorter wavelength band (see Fig. 6f), which

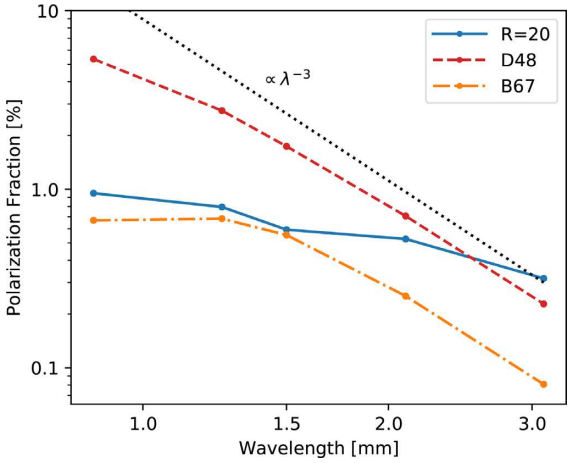

Figure 7. Predicted polarization spectra for the inner disc at 20 au ($R = 20$; blue solid line), the D48 gap (red dashed line), and the B67 ring (orange dash–dotted line) along the major axis. The black dotted line shows a power law that is proportional to λ^{-3}.

reduces the polarization fraction at Band 7 relative to that at Band 6 (Yang et al. 2017). This difference in the shape of the polarization spectrum is characteristic of the scattering-induced polarization in highly structured discs such as HD 163296, and should be searched for through multiwavelength observations. As the wavelength increases further, the ring starts to become optically thin, leading to a drop of the polarization fraction with wavelength, as expected. The inner disc differs from the ring and gap in that it remains optically thick even at the longest wavelength band. Its polarization fraction decreases with wavelength, but rather slowly, approximately as $\lambda^{-0.85}$, which is much shallower than the naive expectation based on Rayleigh scattering. The shallow spectrum is a result of decreasing optical depth with wavelength, which makes the inner disc detectable in polarization at all 5 ALMA bands. The predicted spectrum for the inner disc, if confirmed by future observations, would provide strong evidence supporting the notion that dust scattering is responsible for both polarization and the low spectral index in the region.

4.4 Implications for other discs

As mentioned in the introduction, there is evidence that dust scattering is responsible, at least in part, for the (sub)millimetre polarization detected in an increasing number of discs, with HD 163296, IM Lup, and HL Tau as arguably the best examples. Like HD 163296, IM Lup has polarization data published only in one ALMA band (Band 7, Hull et al. 2018), although data have been taken in Band 6 (ALMA project 2019.1.00035.S, PI: C. Hull). Preliminary results indicate that the Band 6 polarization is also oriented along the disc minor axis (as in Band 7) and that its polarization fraction is higher than that in Band 7 (Hull et al., in preparation). This 'inverted' polarization spectrum (compared with the simple expectation based on Rayleigh scattering) could be indicative of the IM Lup disc being optically thick at both Bands 6 and 7, but more so at Band 7 than Band 6, as illustrated by the B67 curve in Fig. 7. There is an indication that the spectral index α between Band 6 (Cleeves et al. 2016; Andrews et al. 2018) and Band 7 (Cleeves et al. 2016; Hull et al. 2018) is less than 2 in the central region of the disc (within about 50 au), which is independent evidence for strong dust scattering, as is the case for HD 163296.

The HL Tau disc has the most complete published multiwavelength polarization data and spectral index information to date (Kataoka et al. 2017; Stephens et al. 2017; Carrasco-González et al. 2019). In particular, the disc also has rings and gaps and there exists a similar anticorrelation between the Stokes I and spectral index, which suggests varying optical depth as a function of radius, similar to the case of HD 163296. The polarization at Band 7 is mainly along the disc minor axis and thus favours the dust self-scattering explanation at this shortest wavelength band. The polarization at the longest wavelength band (Band 3) has an azimuthal orientation, which complicates the interpretation of scattering-induced polarization, indicating that additional polarization mechanism(s) may be at work[6] (Kataoka et al. 2017; Stephens et al. 2017; Yang et al. 2019). The lowest spectral index between Band 7 and 6 was found to be ∼2 at the rings, which is indicative of an optically thick ring that may or may not be scattering-dominated. Carrasco-González et al. (2019) fitted the spectral energy distributions at different radii including both emission and scattering by spherical grains of power-law size distributions and suggested that the relatively low opacity index ($\beta \lesssim 1$) at small radii requires maximum grain sizes in the millimetre range (see fig. 7). Such grain sizes would be too large to produce the observed polarization orientation, especially in Band 7 (Yang et al. 2016, see their fig. 7). This tension may be alleviated if β at small radii is significantly affected by beam averaging, which can average out the high opacity index ($\beta \sim 2$) from the relatively small (100 μm) grains responsible for scattering-induced polarization in the optically thin gaps and the low apparent opacity index ($\beta \lesssim 0$) from the same (small) grains in optically thick rings (see Fig. 5b for an illustration). Some indication that this may indeed be the case comes from comparing the spectral index between Bands 6 and 7 for the first gap at ∼13 au obtained by ALMA Partnership et al. (2015) at a resolution of 38.6 × 19.3 mas ($\beta \sim 1.1$–1.5, see their fig. 3c) and that by Carrasco-González et al. (2019) at a resolution of ∼50 mas ($\beta \sim 0.5$, see their fig. 3, lower panel). It is plausible that at an even higher resolution β in the gap may increase further, approaching the standard ISM value of 1.7 for small grains even more closely. There is some hint that the spectral index α near the centre is below 2 (see figs 2f and 3c of ALMA Partnership et al. 2015), which provides some additional support to the interpretation of scattering-induced polarization, at least near the centre, as in the HD 163296 case; however, the less-than-two α disappears after smoothing with a larger beam (Carrasco-González et al. 2019). Higher resolution observations and a more detailed analysis of the data are needed to make a firmer case.

5 CONCLUSIONS

In this paper, we have modelled the well-observed protoplanetary disc HD 163296, which has a resolved polarization pattern at ALMA Band 7 ($\lambda = 0.87$ mm) strongly indicative of scattering by ∼ 100 μm grains and an apparently low spectral index between ALMA Band 6 (1.25 mm) and 7, which is traditionally taken as evidence for emission by large, millimetre-sized, grains. As such, it provides an ideal target to investigate the apparent tension between the grain sizes inferred from polarization and spectral index. Our main results are as follows:

[6]Scattering-induced polarization may still be present at Band 3 in HL Tau, but its fraction may be too low (of order 0.3 per cent, see Fig. 6e) to compete with other mechanism(s).

(1) We find that our disc model with grains of sizes up to $a_{\rm max} = 90\,\mu$m broadly reproduces the total intensity (Stokes *I*) observed at 1.25 mm (ALMA Band 6), the spectral index α between 0.87 and 1.25 mm after beam convolution, and the polarization observed at 0.87 mm (see Fig. 5). In particular, the unusually low spectral index $\alpha \sim 1.5$ observed in the inner disc ($\lesssim 30$ au) is reproduced naturally, as a result of the region being optically thick at both wavebands *and* the fact that scattering by the relatively small ($\sim 100\,\mu$m) grains is more efficient at the shorter wavelength; the latter flattens the spectral energy distribution, forcing the spectral index below the Rayleigh-Jeans limit $\alpha = 2$, as pointed out by Liu (2019) and Zhu et al. (2019). We are able to reproduce the spectral index inferred for the two innermost rings and gaps as well, but for a different reason. In our model, the rings are optically thick at both wavebands, with an intrinsic spectral index $\alpha < 2$ as a result of scattering (deviation from the Rayleigh–Jeans power law also contributes to the low α at the outer ring where the temperature is low). The gaps are optically thin, with an intrinsic $\alpha \sim 4$, as expected for small grains. Convolution with the telescope beam brings the spectral index in the rings up, to $\alpha \sim 2$, and that in the gaps down, to $\alpha \sim 2.5$, both of which are broadly consistent with the observationally inferred values (see Fig. 5). The ability for relatively small, 0.1 mm-sized grains to reproduce the spectral index provides a much-needed, independent piece of evidence for scattering-induced polarization in this source, especially in the inner disc where $\alpha < 2$, which is difficult to understand without scattering.

(2) We infer a mid-plane temperature in HD163296 that is close to the ALMA Band 6 brightness temperature at the rings. In order for the ~ 100 μm-sized grains responsible for scattering-induced polarization to reproduce the observed spectral index of $\alpha \sim 2$, we determine that the rings are mostly optically thick. Our inferred mid-plane temperature is lower than that inferred from optically thick CO lines. An implication of this is that the latter likely probe the warmer gas from the disc surface down to the so-called CO snow surface, but not the colder mid-plane region where CO is frozen out.

(3) Rings and gaps in a disc-like HD 163296 produce unique wavelength-dependent patterns in scattering-induced polarization that can be used to further constrain the scattering mechanism. In particular, at shorter wavelengths where the rings are optically thick and gaps optically thin, the polarization fraction is higher in the gaps than in the rings, where the polarization fraction is lowered by large optical depth. Along the gap itself, the polarization is higher along the major axis than along the minor axis (see Fig. 6a). The azimuthal variation is a natural consequence of competition between polarization by radial anisotropy of the radiation field in the gap and polarization by disc inclination. The former is in the azimuthal direction, while the latter is in the direction parallel to the disc minor axis. Together, polarization is enhanced along the disc major axis, but reduced along the disc minor axis. Both the optical depth effect and azimuthal variation are observed in HD 163296 at 0.87 mm (see fig. 1b of Dent et al. 2019). At longer wavelengths where both the rings and gaps are optically thin, the polarization in the rings becomes more prominent relative to that in the gaps, with a higher polarization fraction along the minor axis of the ring (see Fig. 6e); this opposite sense of azimuthal variation is also a consequence of the radiation anisotropy, but in the azimuthal (rather than radial) direction in the rings. Together with polarization induced by disc inclination, polarization is reduced along the major axis, but enhanced along the disc minor axis in the rings.

(4) Scattering-induced polarization has very different spectra across the ALMA Bands (from 0.87 to 3 mm) in rings and gaps. In gaps that are optically thin at all wavebands, the polarization fraction decreases rapidly with increasing wavelength (roughly as λ^{-3}). In the rings, the polarization may increase with increasing wavelength, depending on the optical depth (see Fig. 7). This inversion of polarization spectrum (i.e. higher polarization at longer wavelength) in optically thick rings but not in the neighbouring optically thin gaps is a tell-tale sign of polarization produced by scattering. It should be searched for with high-resolution multiwavelength polarization observations that resolve the disc substructure.

(5) High-contrast substructures such as rings and gaps now commonly observed in protoplanetary discs complicate the use of spectral index α to infer grain sizes unless they are well resolved. If they are not, the telescope beam averages the low and high values of α in the optically thick and thin regions, respectively, into an apparently intermediate α value that may be misinterpreted as evidence for large, millimetre-sized grains. Accounting for beam averaging has the potential to alleviate the tension between the grain sizes inferred from studies of scattering-induced polarization versus that from spectral index studies, but more work is needed to quantify the extent to which it has affected the grain-size estimation in individual sources.

ACKNOWLEDGEMENTS

We express our gratitude to W.R.F. Dent for providing the Band 7 Stokes *I*, polarization, and spectral index profiles of HD 163296, L.I. Cleeves for providing the IM Lup Band 7 and Band 6 continuum images and fruitful discussions, and the DSHARP group for making the radial profiles and images of their data publicly available. We also thank C.P. Dullemond for making RADMC-3D publicly available. We thank the referee for constructive comments. ZDL acknowledges support from ALMA SOS. Z-YL is supported in part by NASA 80NSSC18K1095 and NSF AST-1716259, 1815784, and 1910106. LWL acknowledges support from NSF AST-1910364. CLHH acknowledges the support of both the NAOJ Fellowship as well as JSPS KAKENHI grant no. 18K13586. This paper makes use of the following ALMA data: ADS/JAO.ALMA #2013.1.00226.S, ADS/JAO.ALMA #2013.1.00601.S, ADS/JAO.ALMA #2013.00694.S, ADS/JAO.ALMA #2015.1.00616.S, ADS/JAO.ALMA #2016.1.00484.L, ADS/JAO.ALMA #2016.1.00712.S, and ADS/JAO.ALMA #2019.1.00035.S. ALMA is a partnership of ESO (representing its member states), NSF (USA) and NINS (Japan), together with NRC (Canada), MOST and ASIAA (Taiwan), and KASI (Republic of Korea), in cooperation with the Republic of Chile. The Joint ALMA Observatory is operated by ESO, AUI/NRAO, and NAOJ. The National Radio Astronomy Observatory is a facility of the National Science Foundation operated under cooperative agreement by Associated Universities, Inc.

REFERENCES

ALMA Partnership et al., 2015, ApJ, 808, L3
Alves F. O. et al., 2018, A&A, 616, A56
Andersson B.-G., Lazarian A., Vaillancourt J. E., 2015, ARA&A, 53, 501
Andrews S. M. et al., 2018, ApJ, 869, L41
Armitage P. J., 2015, preprint (arXiv:1509.06382)
Bacciotti F. et al., 2018, ApJ, 865, L12
Balbus S. A., Hawley J. F., 1991, ApJ, 376, 214
Beckwith S. V. W., Sargent A. I., 1991, ApJ, 381, 250
Birnstiel T. et al., 2018, ApJ, 869, L45
Blandford R. D., Payne D. G., 1982, MNRAS, 199, 883
Bohren C. F., Huffman D. R., 1983, Absorption and Scattering of Light by Small Particles, Wiley, New York
Carrasco-González C., et al., 2019, ApJ, 883, 71
Cleeves L. I., Öberg K. I., Wilner D. J., Huang J., Loomis R. A., Andrews S. M., Czekala I., 2016, ApJ, 832, 110

Cox E. G. et al., 2015, ApJ, 814, L28
Dent W. R. F., Pinte C., Cortes P. C., Ménard F., Hales A., Fomalont E., de Gregorio-Monsalvo I., 2019, MNRAS, 482, L29
Draine B. T., 2003, ARA&A, 41, 241
Draine B. T., 2006, ApJ, 636, 1114
Dubrulle B., Morfill G., Sterzik M., 1995, Icarus, 114, 237
Dullemond C. P., Isella A., Andrews S. M., Skobleva I., Dzyurkevich N., 2020, A&A, 633, A137
Fernández-López M., Stephens I. W., Girart J. M., Looney L., Curiel S., Segura-Cox D., Eswaraiah C., Lai S. P., 2016, ApJ, 832, 200
Flaherty K. M., Hughes A. M., Rosenfeld K. A., Andrews S. M., Chiang E., Simon J. B., Kerzner S., Wilner D. J., 2015, ApJ, 813, 99
Flaherty K. M. et al., 2017, ApJ, 843, 150
Gaia Collaboration et al., 2018, A&A, 616, A1
Girart J. M., Rao R., Marrone D. P., 2006, Science, 313, 812
Girart J. M. et al., 2018, ApJ, 856, L27
Gold T., 1952, MNRAS, 112, 215
Harris R. J. et al., 2018, ApJ, 861, 91
Harrison R. E. et al., 2019, ApJ, 877, L2
Henning T., Stognienko R., 1996, A&A, 311, 291
Huang J. et al., 2018, ApJ, 869, L42
Hull C. L. H. et al., 2014, ApJS, 213, 13
Hull C. L. H. et al., 2018, ApJ, 860, 82
Isella A. et al., 2016, Phys. Rev. Lett., 117, 251101
Isella A. et al., 2018, ApJ, 869, L49
Ishimaru A., 1978, Wave Propagation and Scattering in Random Media. Volume 1 – Single Scattering and Transport Theory, Vol. 1, Academic Press, Cambridge, Massachusetts
Kataoka A. et al., 2015, ApJ, 809, 78
Kataoka A., Muto T., Momose M., Tsukagoshi T., Dullemond C. P., 2016a, ApJ, 820, 54
Kataoka A. et al., 2016b, ApJ, 831, L12
Kataoka A., Tsukagoshi T., Pohl A., Muto T., Nagai H., Stephens I. W., Tomisaka K., Momose M., 2017, ApJ, 844, L5
Kataoka A., Okuzumi S., Tazaki R., 2019, ApJ, 874, L6
Kirchschlager F., Bertrang G. H.-M., Flock M., 2019, MNRAS, 488, 1211
Ko C.-L., Liu H. B., Lai S.-P., Ching T.-C., Rao R., Girart J. M., 2020, ApJ, 889, 172
Lazarian A., 1995, ApJ, 451, 660
Lazarian A., Hoang T., 2007a, MNRAS, 378, 910
Lazarian A., Hoang T., 2007b, ApJ, 669, L77
Lee C.-F., Li Z.-Y., Ching T.-C., Lai S.-P., Yang H., 2018, ApJ, 854, 56
Lin Z.-Y. D., Li Z.-Y., Yang H., Looney L., Lee C.-F., Stephens I., Lai S.-P., 2020, MNRAS, 493, 4868
Liu H. B., 2019, ApJ, 877, L22
Mathis J. S., Rumpl W., Nordsieck K. H., 1977, ApJ, 217, 425
Morbidelli A., Raymond S. N., 2016, J. Geophys. Research (Planets), 121, 1962
Mori T., Kataoka A., Ohashi S., Momose M., Muto T., Nagai H., Tsukagoshi T., 2019, ApJ, 883, 16
Ohashi S., Kataoka A., 2019, ApJ, 886, 103
Okuzumi S., Tazaki R., 2019, ApJ, 878, 132
Pohl A., Kataoka A., Pinilla P., Dullemond C. P., Henning T., Birnstiel T., 2016, A&A, 593, A12
Rao R., Girart J. M., Lai S.-P., Marrone D. P., 2014, ApJ, 780, L6
Rosenfeld K. A., Andrews S. M., Hughes A. M., Wilner D. J., Qi C., 2013, ApJ, 774, 16
Sadavoy S. I. et al., 2018a, ApJ, 859, 165
Sadavoy S. I. et al., 2018b, ApJ, 869, 115
Sadavoy S. I. et al., 2019, ApJS, 245, 2
Stephens I. W. et al., 2013, ApJ, 769, L15
Stephens I. W. et al., 2014, Nature, 514, 597
Stephens I. W. et al., 2017, ApJ, 851, 55
Tazaki R., Lazarian A., Nomura H., 2017, ApJ, 839, 56
Tazaki R., Tanaka H., Kataoka A., Okuzumi S., Muto T., 2019, ApJ, 885, 52
Testi L. et al., 2014, in Beuther H., Klessen R. S., Dullemond C. P., Henning T., eds, Protostars and Planets VI. Univ. Arizona Press, Tucson, p. 339
Turner N. J., Fromang S., Gammie C., Klahr H., Lesur G., Wardle M., Bai X. N., 2014, in Beuther H., Klessen R. S., Dullemond C. P., Henning T., eds, Protostars and Planets VI. Univ. Arizona Press, Tucson, p. 411
Vlemmings W. H. T. et al., 2019, A&A, 624, L7
Warren S. G., Brandt R. E., 2008, J. Geophys. Res. (Atmospheres), 113, D14220
Yang H., Li Z.-Y., Looney L., Stephens I., 2016, MNRAS, 456, 2794
Yang H., Li Z.-Y., Looney L. W., Girart J. M., Stephens I. W., 2017, MNRAS, 472, 373
Yang H., Li Z.-Y., Stephens I. W., Kataoka A., Looney L., 2019, MNRAS, 483, 2371
Zhu Z. et al., 2019, ApJ, 877, L18

APPENDIX A: AN ILLUSTRATIVE MODEL OF A WARMER DISC

To illustrate the effects of a higher temperature, we adopt the temperature profile of Flaherty et al. (2015) (see Fig. 5e) and vary the surface density parameters to fit the Band 6 Stokes *I* high-resolution image. The parameters are shown in Table A1. The resulting major axis profiles are plotted in Fig. A1, as in the standard model shown in Fig. 5.

With a higher temperature, the optical depth in Band 6 (Fig. A1d) has to decrease to reach the same flux. As a result, the B67 and B100 are no longer optically thick, which pushes the spectral index α well above the observational constraint.

We can see in Fig. A1(c) that the non-convolved polarization fraction in Band 7 in the gaps for the warmer model is lower than that for the standard model. This is expected since polarization increases with optical depth in the optically thin limit and the optical depth in the gaps for the warmer model is lower than that for the standard model. On the other hand, the polarization in the rings drop to a similar value for both models. The low value of polarization spans a larger region for the standard model, which can be understood since the polarization fraction is roughly constant in the optically thick limit and the rings of the standard model have a larger region where they are optically thick (see Fig. A1d). After convolution, the polarization fractions from both models appear roughly similar.

Table A1. A chosen set of parameters for the warmer model formatted in the same way as Table 2.

Parameters				
R_t (au)	124			
T_t (K)	22.5			
q	0.3			
H_t (au)	3			
B2				
Power-law-like surface density				
Feature	Inner disc	D48	D86	B100
$\Sigma_{p,0}$ (g cm^{-2})	7	0.02	0.06	0.2
p	0.3	0	0	6
R_a (au)	0.5	38	76	105
R_b (au)	26	58	96	135
σ_a (au)	0	5	5	5
σ_b (au)	6	4.5	5	10
B2				
Gaussian-like surface density				
Feature	B67	B100	B155	
$\Sigma_{G,0}$ (g cm^{-2})	0.9	0.3	0.04	
R_0 (au)	67	100	155	
σ_c (au)	5	3	5	
σ_d (au)	5	4	25	

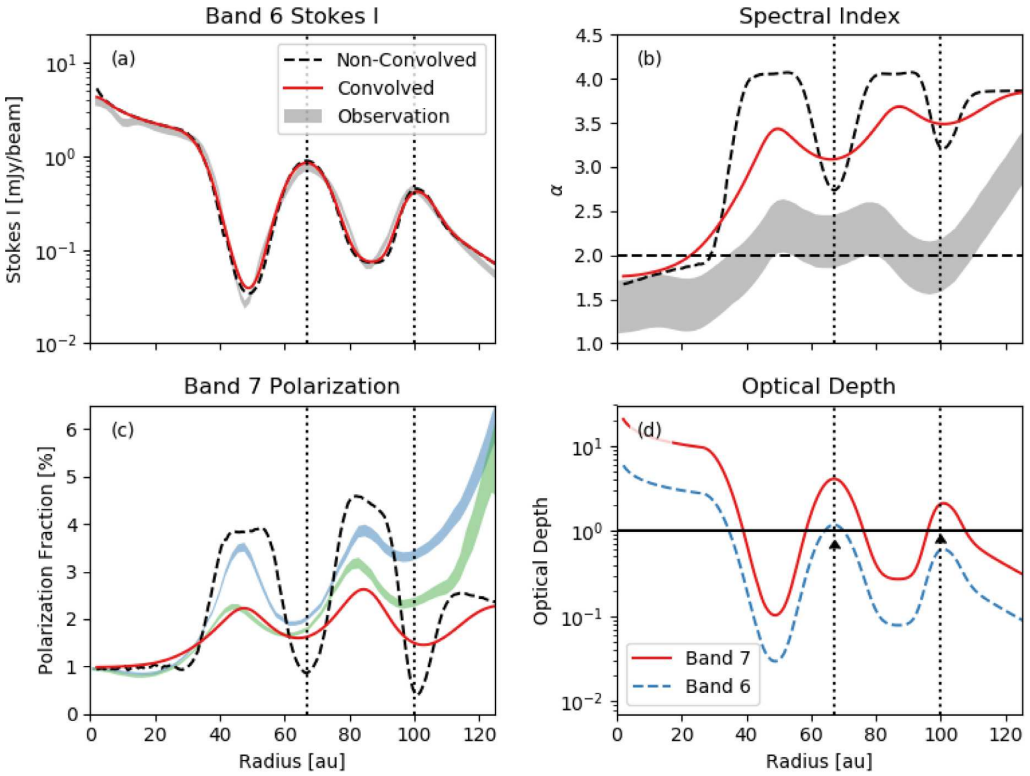

Figure A1. Major axis profiles for the model using a warmer mid-plane temperature from Flaherty et al. (2015). Panels (a)–(d) are plotted in the same way as Figs 5(a)–(d).

This paper has been typeset from a TEX/LATEX file prepared by the author.